

PFC/JA-88-31

Whistler Instability in an ECRH,
Mirror-Confined Plasma

R. C. Garner[†], M. E. Mauel[‡], S. A. Hokin*,
R. S. Post, and D. L. Smatlak

August 30, 1988

Plasma Fusion Center
Massachusetts Institute of Technology
Cambridge, Massachusetts 02139 USA

Submitted for publication to *The Physics of Fluids*.

[†]Current address: PhotoMetrics, Inc., 4 Arrow Dr., Woburn, MA.

[‡]Current address: Dept. of Applied Physics, Columbia University, New York, NY.

*Current address: Dept. of Physics, University of Wisconsin, Madison, WI.

Whistler Instability in an ECRH, Mirror-Confined Plasma

R. C. Garner ^a, M. E. Mauel ^b, S. A. Hokin,
R. S. Post, and D. L. Smatlak

Plasma Fusion Center
Massachusetts Institute of Technology
Cambridge, Massachusetts 02139

August 30, 1988

Abstract

The warm electron driven (2 keV) whistler electron microinstability [1] of the Constance B electron cyclotron resonance heated (ECRH), quadrupole mirror confined plasma experiment has been studied. Experiments show 1) the instability comes in fairly regular bursts on axis and continuously in time off axis due to the minimum B geometry, 2) a frequency spectrum which is insensitive to changes in the plasma parameters, and 3) instability induced power losses which are not greater than 10% of the ECRH power input for the regimes studied. A linear perturbation analysis of the relativistic Vlasov equation together with Maxwell's equations has been made. Using the ECRH distribution function, a new distribution function [1] well suited for describing ECRH, mirror confined plasmas, the analysis shows the instability frequency spectrum to be insensitive to changes in cyclotron frequency, temperature, and density, in agreement with experimental results, and only sensitive to changes in ECRH frequency.

1 Introduction

The whistler instability is an electron microinstability which is driven by temperature anisotropy of the electron velocity space distribution. It is well known that a mirror-confined plasma, which is inherently anisotropic if the electrons are heated to energies greater than the plasma potential, may be whistler unstable. Unstable microwave emission in a regime near the electron cyclotron frequency has been observed and characterized in a wide variety of mirror experiments.[2,3,4,5,6] Theoretical investigations using linear perturbation theory and models for the electron velocity distribution have been made and used to identify the whistler instability.[7,8,9]

We have investigated the whistler instability which exists in the Constance B electron cyclotron resonance heated (ECRH), mirror-confined plasma. In a previous paper we showed that the whistler instability in this plasma is driven by the warm electron component (2 keV), while the hot electron component (450 keV) is microstable. [1] We also showed that this agrees well with a linear perturbation analysis using the ECRH distribution, a new distribution function that is well suited to describing ECRH, mirror- confined plasmas.

In this paper we show the effects that the whistler instability has on the Constance B plasma. Section 2 presents experimental observations. The radial behavior of the instability in the inhomogeneous magnetic field is described. The frequency spectrum is shown to be insensitive to changes in the parameters which are variable in the experiment. Power losses due to unstable rf emission and instability induced electron endloss are shown to be less than 10% of the ECRH power input for the conditions investigated. Section 3 presents conclusions from the linear perturbation analysis using the ECRH distribution. We show that the predicted whistler frequency spectrum is only dependent on the ECRH frequency and insensitive to changes in cyclotron frequency, plasma density, and plasma temperature. We deduce an explanation for the radial behavior of the whistler instability observed in experiments.

2 The Constance B Experiment

Constance B is a single-cell, minimum B magnetic mirror in which the plasma is created and the electrons are resonantly heated by microwaves. A baseball seam shaped coil produces a quadrupole magnetic field with constant $|\mathbf{B}|$ surfaces which are egg-shaped. A klystron supplies up to 5 kW of microwave power at 10.5 GHz. A typical value of $|\mathbf{B}|$ at the midplane on the axis is 3 kG, which makes a nonrelativistic resonance zone of length 30 cm and radius 10 cm.

The principal diagnostics used for this work consist of 1) a linear array of five gridded, electrostatic endloss analyzers for endloss energies less than 5 keV, 2) an rf receiving system for measuring the total power and the frequency spectrum between 5.5 GHz and 18 GHz, 3) a diamagnetic loop at the midplane to measure plasma stored energy, 4) hard and soft x ray detectors to measure electron temperature, 5) a scintillator probe to measure high energy (> 100 keV) electron endloss, and 6) an interferometer to measure the line integrated density.

A typical plasma shot for whistler instability studies is depicted in Fig. 1. The ECRH power, the neutral gas pressure and the magnitude of the magnetic field are directly controllable. The ECRH power and the magnetic field may be on for as long as 10 sec.

2.1 Description of Plasma

The Constance B plasma parameters are characterized by slowly varying equilibrium values superimposed by faster fluctuations which are identified as whistler instability (see Fig. 2). The whistler fluctuations, which are discussed in the next section in detail, consist of bursts of rf emission which correlate with bursts of electron and ion endloss, and diamagnetism and potential fluctuations.

The equilibrium plasma parameters are summarized in Table I. The plasma is characterized by a three component electron energy distribution function. The cold and warm component temperatures are measured with the gridded, electrostatic endloss analyzers. The hot component temperature is measured with the x ray detectors. The diamagnetism and x ray detectors are used to determine the hot electron density. Since the hot electron collisional confinement time is greater than

1000 times that of the cold electrons, the cold electron density is determined by considering the difference between interferometer measurements while ECRH is applied and after ECRH is turned off. A relativistic approximation is used in determining hot electron density with interferometer measurements [6]. The soft x ray detectors do not detect the whistler unstable warm component, which provides the upper limit on warm electron density.

2.2 Description of Whistler Instability

2.2.1 General Behavior

The bursts of rf emission and associated fluctuations are identified as electron microinstability because the rf emission frequencies are near the electron cyclotron frequencies and the rf bursts correlate with bursts of electron endloss.

There are two types of unstable rf emission. We refer to the regular bursting type of emission shown in Fig. 2 as whistler B emission. Figure 3 shows an example of a shot in which the rf burst rate is highly irregular or continuous. We refer to this type of emission as whistler C emission. Whistler C emission is generally observed for intermediate ranges of neutral gas pressure and/or high ECRH powers. For example, for an ECRH power of 1 kW and a midplane magnetic field of 3 kG, whistler C emission is present when the neutral gas pressure is in the range 7×10^{-7} Torr to 2×10^{-6} Torr. Whistler B emission is present in this regime as well, but at lower frequencies. Above this pressure regime the whistler C emission power is much lower than the whistler B emission power. For high enough ECRH power (> 2 kW) and high enough magnetic field (> 2.5 kG) whistler C emission is always more prevalent than whistler B emission, independent of pressure. However, at low magnetic fields there is no whistler C emission.

A study of this rather complicated qualitative behavior of the rf emission in conjunction with electron endloss measurements at different radii shows that the whistler C emission, when present, is associated with plasma off axis while the whistler B emission is associated with the on axis plasma. These studies also indicate that both types of emission are due to the same microinstability. The behavior of the plasma at different radii from the axis is observed with the five endloss analyzers

which are located symmetrically about the axis at 6 cm intervals along the thin part of the plasma fan on one end of the vacuum chamber. Figure 4 shows data from the five endloss analyzers for a shot in which both whistler B and whistler C emission is observed. The analyzers were set to measure total current due to electrons with energies greater than 30 eV (30 volts is the bias needed to suppress secondary electrons from being emitted from the analyzer collector). The ECRH power was 1 kW and the magnetic field was 2.8 kG. Analyzers at 0 and +6 cm clearly show a regular bursting behavior just like the whistler B emission. The outer analyzers at +12, -6, and -12 cm show an irregular bursting current just like the whistler C emission. Figure 5 shows the type of emission observed as the magnetic field is changed, with pressure and ECRH power remaining constant. As the magnetic field is increased, plasma originally on outer field lines for lower fields is brought inward toward the axis. The opposite effect occurs as the magnetic field is decreased. Thus, for a shot in which the magnetic field is 2.4 kG and with the same ECRH power and neutral gas pressure, regular bursting occurs on all the endloss analyzers. For a shot in which the magnetic field is 3.6 kG and with the same ECRH power and neutral gas pressure, analyzers +12, -6, and -12 show no endloss while analyzers 0 and +6 show irregular whistler C type bursting. In addition, when the magnetic field is 3 kG, the ECRH power is 1 kW, and the neutral pressure is below 7×10^{-7} Torr analyzers +12, -6, and -12 show no endloss while analyzers 0 and +6 show regular whistler B type bursting. It was stated previously that there is no whistler C emission for such a shot.

Higher density at the outer radii may be the reason why whistler C is emitted there. Smatlak, et al., [12] have shown that the equilibrium density contours of a baseball mirror are shaped like the baseball seam, with the maximum density occurring on the curve defined by $f_{ECRH} = f_{ce}$. The linear perturbation theory with the ECRH distribution described in the next section predicts higher unstable wave growth rates for higher total density (Fig. 18). A quasilinear calculation [13] describing the time evolution of the equilibrium electron distribution function in a magnetic mirror has shown that the whistler instability emission changes from bursting to continuous as the growth rate is increased.

2.2.2 Frequency Spectrum

Figure 6 shows the frequency regime of the total unstable rf emission for three different magnetic fields. These data were taken for a shot in which the ECRH power was 3 kW and the neutral gas pressure was 1×10^{-6} Torr, conditions for which whistler C and whistler B emission are present. Figure 7 shows the frequency regime for different magnetic fields when only whistler B emission is present. Three observations to note from these data are 1) the frequency spectrum is not a strong function of magnetic field, 2) the spectrum extends to higher frequencies when the whistler C emission is present, and 3) the frequencies are below the ECRH frequency of 10.5 GHz (unstable frequencies greater than 10.5 GHz have never been observed for any of the parameter regimes studied). These observations are predicted by dispersion relation calculations which will be presented in Section 3.

2.2.3 Whistler Instability Effects on Power Balance

Power loss due to whistler instability is primarily by rf emission and electron endloss. Instability induced ion endloss accounts for less than 10% of the instability induced power loss because of the lower ion energies and will therefore not be discussed.

2.2.3a rf Emission

Figure 8a shows the measured unstable rf power as a function of neutral gas pressure for an ECRH power of 1 kW and a midplane magnetic field of 3 kG. The behavior is qualitatively the same for other ECRH powers, with the maximum unstable rf emission always occurring at the same pressure of 1×10^{-6} Torr. The instability induced electron endloss also peaks at this pressure, as is shown below in Fig. 10. Figure 8b shows a plot of the maximum value of unstable rf power and the maximum value of unstable rf power divided by the plasma diamagnetism, both as a function of ECRH power. For ECRH powers below 1 kW both graphs are linear, as is a plot of the diamagnetism versus ECRH power. Between 1 kW and 3 kW (3 kW is the highest ECRH power used for this investigation) the unstable rf power normalized to the diamagnetism is linear.

The measured rf emission can be related to the actual power emitted by the plasma because of the rf cavity effects of the vacuum chamber. Experimental jus-

tification of the cavity-like nature of the vacuum chamber has been made and was presented in [6]. The actual power emitted by the plasma is linearly related to the power measured at some location at the vacuum chamber wall. The constant of proportionality is determined by measuring the response of the rf detection system to a test wave of known power put into the chamber. Table II shows the peak power loss due to whistler rf emission for an ECRH power of 1 kW and a midplane magnetic field of 3 kG.

2.2.3b Electron Endloss

In our previous paper we established the fact that the warm electrons drive the whistler instability but that both warm and hot electrons are lost when the instability is present. Therefore, determining the power loss due to electron endloss requires a measure of the energy distribution of both types of endloss. Figure 9 shows the total axial electron endloss energy distribution up to 5 keV (measured with the gridded electrostatic endloss analyzers). The curve is approximately the sum of two Maxwellian distributions with two different temperatures. The lower temperature (250 eV) corresponds primarily to collisional endloss. The higher temperature (2 keV) corresponds to instability induced endloss plus endloss induced by the interaction of the electrons with the ECRH waves. ECRH induced endloss can be subtracted out using the 2 keV endloss component which exists between bursts (assuming that the endloss between bursts is primarily due to interactions with the ECRH waves and is the same as during the bursts). Hokin [14] has done this and has shown that the ECRH induced endloss is approximately equal to the instability induced endloss for the 2 keV electron component. The high instantaneous instability induced endloss is concentrated in the relatively short time duration bursts whereas the ECRH induced endloss persists at a lower level during the entire shot.

Plots similar to the one in Fig 9 for other ECRH powers, pressures, and magnetic fields always show an energy distribution for the instability induced electron endloss with an average energy in the range of 1.5 to 2.5 keV. Thus, the warm electron temperature is not sensitive to changes in the experimental conditions. However, the absolute number of electrons lost is affected. Figure 10 shows the electron endloss current for electrons with energies greater than 500 eV as a function of pressure for an ECRH power of 1 kW and a magnetic field of 3 kG. These data

were taken for the same shots used for Fig. 8. Note that the endloss current peaks at the same pressure as the unstable rf emission.

The endloss analyzers off axis were used to determine the radial behavior of the instability induced electron endloss. The information is used to determine the total power loss in the form of warm electron instability induced endloss. This is given in Table II.

The hot electron endloss is observed with a scintillator probe located on axis. The electron endloss due to microinstability is distinguished from the equilibrium endloss (mainly due to the interaction with ECRH waves for these high energies) by doing shots like the one depicted in Fig 11. This shot is composed of three parts. The first part is like any typical plasma shot, with constant gas pressure and constant ECRH power. The hot electron endloss is caused by the microinstability, collisions, and electron interactions with the ECRH waves. For the second part the ECRH and gas are turned off. This causes only a hot component to be left after the few milliseconds that it takes for the cold and warm components to decay. During this phase of the shot the measured hot electron endloss is due to collisions only because the microinstability stops after warm electrons have decayed by a suitable amount (approximately 5 msec). The third part of the shot has a second ECRH pulse but still no gas. With no buildup of a warm plasma possible, there is no microinstability. Here the measured hot electron endloss is due to collisions and interaction with ECRH waves.

From these shots it is possible to determine the relative importance of the three processes which cause hot electron endloss. This is shown in Table II. The radial behavior of the hot electron endloss was assumed to be the same as the radial behavior of the warm electron endloss.

Table II is a summary of the microinstability induced power losses from the Constance B plasma. There are several uncertainties in this table. There is a 25% uncertainty in the calibration factor for the rf emission power. The instability induced hot electron endloss radial profile was assumed to be the same as the instability induced warm electron endloss. The ECRH induced hot electron endloss radial profile was taken to be constant over the 20 cm diameter cross section of the plasma.

3 Theoretical Analysis of Microinstability

3.1 Model

Dispersion relation calculations are based on the linear perturbation analysis of the relativistic Vlasov equation (for electrons) together with Maxwell's equations for an infinite, homogeneous medium (the results of the calculations show these assumptions to be valid for the Constance B experiment, as is shown below). The ions are taken to be stationary and only contribute in neutralizing the plasma. The electric field is assumed to have the form $\mathbf{E}(\mathbf{k}, \omega) \exp[i(\mathbf{k} \cdot \mathbf{r} - \omega t)]$, where \mathbf{k} is real, $\omega = \omega_r + i\omega_i$, and $\omega_i \ll \omega_r$. The quantity of interest is the temporal growth rate ω_i which is calculated in the following manner[10]:

$$\omega_i = - \frac{\mathbf{E}^* \cdot \mathbf{D}^a \cdot \mathbf{E}}{\mathbf{E}^* \cdot \frac{\partial \mathbf{D}^h}{\partial \omega_r} \cdot \mathbf{E}} \quad (1)$$

where \mathbf{E}^* is the Hermitian conjugate of the electric field amplitude \mathbf{E} , and \mathbf{D}^a and \mathbf{D}^h are respectively the anti-Hermitian part and the Hermitian part of the relativistic Vlasov dispersion tensor.

The Hermitian part of the dispersion tensor is approximately equal to the cold, fluid dispersion tensor if the cold electron component density is much greater than the warm and hot electron component densities. We have made this assumption in our analysis to simplify the calculations. Therefore, our analysis considers only the contribution that resonant particles have on stability. It does not consider the effects of negative energy waves which either enhance instability that would otherwise exist due to resonant particles or cause instability in regimes which would otherwise be stable. With this assumption the denominator of Eq. 1, which is recognized as the wave energy density, is always positive. Instability occurs if the numerator is less than zero.

Our analysis has consisted of choosing a value for ω_r and θ_k , the angle between the wave vector and the magnetic field, solving for \mathbf{k} using the cold plasma dispersion relation, and determining ω_i using Eq. 1. \mathbf{D}^a has been reduced to the following form:

$$\mathbf{D}^a = -2\pi^2 \frac{\omega_p^2}{\omega^2} \int_{L_1}^{L_2} du_{\parallel} \left[\left(\frac{\partial}{\partial \gamma} + \frac{k_{\parallel}}{\omega} \frac{\partial}{\partial u_{\parallel}} \right) f_0 \times \sum_{n=-\infty}^{\infty} \mathbf{T}_n \left(\frac{k_{\perp} u_{\perp}}{\omega} \right) \right]_{\gamma = \frac{k_{\parallel} u_{\parallel} + n}{\omega}} \quad (2)$$

where $u_{\parallel} = v_{\parallel}\gamma/c$, $u_{\perp} = v_{\perp}\gamma/c$, $\gamma = (1 + \mathbf{u}^2)^{1/2}$, $\omega = f/f_{ce}$, $\omega_p = f_p/f_{ce}$, f_{ce} is the electron cyclotron frequency, the wave vector \mathbf{k} is normalized to ω_{ce}/c , f_0 is the equilibrium electron distribution function, and \mathbf{T}_n is a tensor which is given in reference [8]. The limits of integration, L_1 and L_2 , are the positive solutions to

$$\left(\frac{k_{\parallel}^2}{\omega^2} - 1\right) u_{\parallel}^2 + \frac{2nk_{\parallel}}{\omega^2} u_{\parallel} + \left(\frac{n^2}{\omega^2} - 1\right) = 0 \quad (3)$$

arranged such that $L_1 < L_2$. The meaning of these limits as well as a pictorial representation of the integral in Eq. 2 is shown in Fig. 12.

Equation 2 is the result of writing \mathbf{D}^a in the variables u_{\parallel} and γ and then performing the resulting integral over γ . This can be done without an explicit form for f_0 , the distribution function, since the integrand has a simple pole in the variable γ . This is reflected by the fact that the remaining integral is performed with γ replaced by $(k_{\parallel}u_{\parallel} + n)/\omega$, which is the resonance condition. The remaining integral is performed numerically once a distribution function is chosen. Only the fundamental harmonic resonance between the particles and waves ($n = 1$) is considered.

3.2 ECRH Distribution Function

In our previous paper we introduced the ECRH distribution which we use to model the warm electron component of the plasma. The ECRH distribution function is chosen to reflect the expected stochasticity of the the warm electrons in Constance B with respect to the ECRH waves. Thus, it was chosen so that it would have a similar qualitative appearance to distribution functions which result from Fokker-Planck calculations of mirror-confined, ECRH plasmas.

The ECRH distribution is given by

$$f_0(E, \mu) = \exp\left[-\frac{\chi}{T_{\chi}} - \theta(\eta) \frac{\eta}{T_{\eta_+}} + \theta(-\eta) \frac{\eta}{T_{\eta_-}}\right] \quad (4)$$

where $\chi = \frac{1}{2}(E + \mu B_h)$, $\eta = \frac{1}{2}(E - \mu B_h)$, $E = mc^2(\gamma - 1)$ is the particle kinetic energy, $\mu = \frac{1}{2}mu^2/B$ is the magnetic moment, $\theta(\eta)$ is the unit step function, $B_h = \omega_h m_o c/e$, and ω_h is the applied ECRH frequency. T_{χ} , T_{η_+} , and T_{η_-} are constants which we refer to as the temperatures. Useful descriptive quantities are the ratios T_{χ}/T_{η_+} and T_{χ}/T_{η_-} . As these ratios approach infinity the contours of the ECRH

distribution function approach the family of curves which represent the quasilinear diffusion paths corresponding a wave of frequency ω_h .

The inhomogeneity of the magnetic field along the axis is included in the above calculation by way of the normalization of the distribution function. The distribution function is normalized to unity at the midplane. Normalization at other axial locations along a given field line is then made by mapping the distribution function from the midplane using the unperturbed single particle orbits as a transformation. This has the effect of causing the electron density to vary along a field line. In addition, the density is multiplied by the local mirror ratio to reflect the increase in density due to the compression of the magnetic flux.

3.3 Results

The maximum unstable frequencies occur for $\theta_k = 0$ on the R-X branch of the dispersion relation (the terminology used to describe the cold plasma waves follows that given in reference [11]). These are pure whistler waves. Therefore, in what follows only $\theta_k = 0$ is considered. Figure 13 shows a plot of the contours of $f_i = \omega_i/2\pi$ as a function of wave frequency f_r and local cyclotron frequency f_c for particular choices of temperature parameters. These temperatures were chosen because they give an average energy ($\frac{1}{2}m \int v^2 f dv$) of 2.5 keV. It is seen that the maximum unstable frequencies agree well with those observed in the experiment (see Figs. 6 and 7). Other distribution functions, such as the bi-Maxwellian and loss cone distributions predict unstable frequencies which are approximately 2–3 GHz lower than those predicted with the ECRH distribution and thus do not agree well with experiment.[6] Using the bi-Maxwellian distribution the well known sufficient condition for whistler instability is

$$f_r < \left(1 - \frac{T_{\parallel}}{T_{\perp}}\right) f_c \quad (5)$$

Using the ECRH distribution a necessary condition for whistler instability is found

$$f_r < \left(\frac{T_x - T_{\eta+}}{T_x + T_{\eta+}}\right) f_h \quad (6)$$

Equation 6 is derived by using the ECRH distribution in the nonrelativistic version of Eq. 2 and with $\theta_k = 0$. Equation 6 indicates that whistler instability can only

occur for frequencies below the ECRH frequency. This fact agrees with experiment.

The result of Fig 13 is not sensitive to choice of the temperature parameters T_χ , $T_{\eta+}$, and $T_{\eta-}$ for average energies in the warm electron energy regime. Figures 14 and 15 show plots of the maximum unstable frequency regime (the regime bounded by the two half maxima on either side of the maximum) as a function of T_χ , holding $T_\chi/T_{\eta+}$ and $T_\chi/T_{\eta-}$ constant (Fig 14), and as a function of $T_\chi/T_{\eta+}$, holding $T_{\eta+}/T_{\eta-}$ constant (Fig 15). These figures show that the maximum unstable frequencies do not change much below a certain average energy. Of course, the value of f_i does change, first increasing with average energy, and then decreasing. Above some average energy the plasma is stable, a result of the relativistic model. The average energy as a function of the temperature parameters is shown in the final plot in each figure. This lack of sensitivity to changes in the temperature parameters is reflected in the experiment by the fact that the unstable frequency regime does not change during the shot, even during plasma buildup and plasma decay (as long as instability is present). Also, for dispersion relation calculations this result is fortunate since it suggests that, in describing the warm electrons, it is not necessary to know precisely the values of the temperature parameters. For the hot electrons stability is predicted by the calculations and is observed experimentally.

Figure 16 shows that the maximum unstable frequency regime is not sensitive to changes in the midplane cyclotron frequency. This also agrees well with experiment (see Figs. 6 and 7). This is not a property of a plasma which has a bi-Maxwellian or loss cone distribution in which the unstable frequencies are related to the cyclotron frequency as indicated by the inequality in Eq. 5.

The maximum unstable frequency regime is only sensitive to changes in the ECRH frequency when the ECRH distribution is used, as shown in Fig. 17 and as indicated by the inequality in Eq. 6. This has not been measured in Constance B due to the unavailability of different ECRH sources.

Figure 18 shows a plot of the maximum unstable frequency regime as a function of total midplane electron density, with the ratio of warm electron density to total electron density held constant. It is seen that the growth rates increase with total density and the unstable frequency regime is wider. It was mentioned earlier that this may explain the difference between the whistler B and whistler C emission.

3.4 Justification of Model

The results shown in Figs. 14 through 18 justify the simplifying assumptions made in the model we have used (infinite, homogeneous plasma and $\omega_i \ll \omega_r$). In each of these figures plots of k_r and $k_i = \omega_i/v_g$ are included. It is seen that the calculated wavelengths of the maximally unstable waves are typically less than 1 cm. This is to be compared to the 30 cm length (on axis) of the ellipsoidal resonance zone in Constance B. The magnetic field changes by a factor of 1.25 over 15 cm of length at the magnetic well, which gives an average $B/\frac{dB}{dt}$ of 60 cm. In addition, the density along the magnetic field line for an ECRH distribution function changes by less than 10% within the resonance zone, which is where the theoretically predicted instabilities always occur.

For the infinite and homogeneous medium assumptions to be valid the growth rates must be much greater than the bounce frequency so that an electron does not sample a large portion of space during a growth time. The bounce frequency in a magnetic field approximated by a parabolic well is $f_b = v_{\perp o}/2\pi L$, where $v_{\perp o}$ is the midplane perpendicular velocity and L is the mirror length, chosen here to be 30 cm so that the resonance zone is in the correct location corresponding to Constance B. For a 2 keV particle $f_b=14$ MHz, which is much less than a typical calculated growth rate. For a 400 keV particle $f_b=130$ MHz, assuming the perpendicular energy is the total energy.

4 Conclusions

The warm electron driven whistler electron microinstability of the Constance B ECRH, quadrupole mirror confined plasma has been studied. Experiments show 1) there is a change from bursting to continuous unstable whistler emission for increasing distance from the axis, 2) the unstable frequency spectrum is insensitive to changes in the plasma parameters, and 3) instability induced power loss is less than 10% of the ECRH power input for the regimes studied. A linear perturbation analysis of the relativistic Vlasov equation together with Maxwell's equations has been made. Using the ECRH distribution function the analysis shows the instability frequency spectrum is insensitive to changes in cyclotron frequency, temperature, and density

and only sensitive to changes in ECRH frequency. The analysis also suggests that the radial behavior of the whistler instability is due to the increase in density which is caused by the minimum B geometry.

This work was supported by the U.S. Department of Energy, under Contract No. DE-AC02-78ET51013.

References

- (a) Current address: PhotoMetrics, Inc., 4 Arrow Dr., Woburn, MA 01801.
- (b) Current address: Dept. of Applied Physics, Columbia University, New York, N.Y. 10027.
- [1] R. C. Garner , M. E. Mauel, S. A. Hokin, R. S. Post and D. L. Smatlak, *Phys. Rev. Lett.* **59**, 1821 (1987).
- [2] R. A. Blanken and N. H. Lazar, *Phys. Fluids* **13**, 2752 (1970).
- [3] H. Ikegami, H. Ikezi, M. Hosokawa, K. Takayama, and S. Tanaka, *Phys. Fluids* **11**, 1061 (1968).
- [4] R. A. James, R. F. Ellis and C. J. Lasnier *Bulletin of the American Physical Society*, **29**, 1187 (1984).
- [5] J. H. Booske, W. D. Getty, and R. M. Gilgenbach, *Phys. Fluids* **28**, 3116 (1985).
- [6] R. C. Garner, Ph.D. thesis, Massachusetts Institute of Technology, (1986).
- [7] Y. Y. Lau and K. R. Chu, *Phys. Rev. Lett.* **5**, 243 (1983).
- [8] H. K. Wong, C. S. Wu, F. J. Ke, R. S. Schneider, and L. F. Zieball, *Plasma Physics*, **28**, 503 (1982).
- [9] L. C. Lee and C. S. Wu, *Phys. Fluids* **23**, 1348 (1980).
- [10] Bers A. *Plasma Physics—Les Houches 1972* (Gordon and Breach Science Publishers, New York, 1972).
- [11] T. H. Stix, *The Theory of Plasma Waves* (McGraw Hill, New York, 1962).
- [12] D. L. Smatlak, X. Chen, B. G. Lane, S. A. Hokin and R. S. Post, *Phys. Rev. Lett.* **58**, 1853 (1987).
- [13] P. A. Bespalov, *Physica Scripta*, **12**, 576 (1982).
- [14] S. A. Hokin, Ph.D. thesis, Massachusetts Institute of Technology, (1987).

Tables

$T_{e,cold}$:	150 eV
$T_{e,warm}$:	1.5–2.5 keV
$T_{e,hot}$:	450 keV
$\langle n_{e,cold} \rangle$:	$2.0 \times 10^{12} \text{ cm}^{-2}$
$\langle n_{e,hot} \rangle$:	$1.0 \times 10^{12} \text{ cm}^{-2}$
$n_{e,warm}$:	$< 0.1 \times n_{e,hot}$
T_i :	20–30 eV
ϕ_p :	150 volts
plasma length:	30 cm
plasma diameter:	20 cm

Table I: Equilibrium plasma parameters

ECRH input power:	1 kW
estimated ECRH power absorbed [14]	600 W
cold electron endloss:	24 W
warm electron endloss (microinstability):	80 W
hot electron endloss (microinstability):	90 W
hot electron endloss (ECRH)	280 W
unstable rf emission:	40 W

Table II: Summary of power losses due to microinstability.

Figure Captions

Fig. 1. A typical plasma shot with 1 kW of ECRH power, 3 kG midplane magnetic field, and 1×10^{-6} torr neutral gas pressure. The ECRH is turned on at 0.25 sec and turned off at 2.0 sec. a) Microwave power using an open ended X band waveguide at the midplane. Most of the signal is due to the 10.5 GHz ECRH power. b) Line density using the interferometer. c) Diamagnetism. d) Electron endloss current density on axis. e) Total unstable rf emission using the same waveguide as above but with a 10.5 GHz notch filter with 60 db rejection and 15 MHz spread.

Fig. 2. a) Total unstable rf emission (whistler B emission) for 1 kW ECRH power, 3 kG magnetic field, and 7×10^{-7} Torr neutral gas pressure. b) Unstable rf emission and c) electron endloss on an expanded time scale showing the correlation of fluctuations.

Fig. 3. a) Total unstable rf emission (primarily whistler C emission) for 3 kW ECRH power, 3 kG magnetic field, and 1×10^{-6} Torr neutral gas pressure. b) Unstable rf emission and c) electron endloss on an expanded time scale. The rf emission is continuous whereas the (on axis) endloss contains discrete bursts, a phenomenon described later in the text.

Fig. 4. Electron endloss current density from the five endloss analyzers on one end of the machine. The analyzers are in a line along the thin dimension of the plasma fan at positions a) -12 cm, b) -6 cm, c) 0 cm, d) +6 cm and e) +12 cm. A given radial dimension at the wall maps approximately to the same radial dimension at the midplane. ECRH power is 1 kW. Neutral gas pressure is 1×10^{-6} torr. Midplane magnetic field is 2.8 kG.

Fig. 5. Emission type vs magnetic field as observed with the five endloss analyzers. ECRH power is 1 kW. Neutral gas pressure is 1×10^{-6} torr.

Fig. 6. Upper and lower cutoff frequencies for conditions when both the whistler B emission and whistler C emission are present. The points indicate the fields for which data were taken.

Fig. 7. Upper and lower cutoff frequencies for conditions when only whistler B emission is present. The points indicate the fields for which data were taken.

Fig. 8. a) Power of total unstable rf emission vs a) pressure with 1 kW ECRH power b) ECRH power with 1×10^{-6} Torr neutral gas density. In both cases the midplane magnetic field is 3 kG. Each point is the average over a 40 msec time window during different shots with identical machine parameters.

Fig. 9. Energy distribution of the electron endloss observed with the electrostatic gridded endloss analyzers. Two different average energies are observed. Each point corresponds to the average current (mapped to the midplane) over a 40 msec time window at identical times during different shots. The warm component endloss current consists of bursts due to microinstability and an average level which exists both during and between bursts.

Fig. 10. Electron endloss with energies greater than 500 eV vs neutral gas pressure observed with analyzers at a) -6 cm, b) 0 cm and c) +6 cm.

Fig. 11. a) Line density, b) diamagnetic flux, c) unstable rf emission power and d) electron endloss power for a two pulse ECRH shot. The ECRH is turned on the first time at 0.25 sec. and turned off at 1.2 sec. The neutral gas is turned off at 1.4 sec also. The ECRH turned on again 1.7 sec and turned off at 1.9 sec after which it is left off. Note the lack of unstable rf emission during the second pulse where there is only a hot electron population.

Fig. 12. Diffusion paths in the γ - u_{\parallel} plane for a) $\omega/\omega_{ce} < 1$ and b) $\omega/\omega_{ce} > 1$. The limits of the integral in Eq. 2 are the intersections of the resonant particle line with the boundary of the physically meaningful portion of this space. The lack of an intersection gives a limit of infinity. The lack of any intersection means no resonant particles and therefore no instability.

Fig. 13. Contours of f_i . The vertical axis is the local cyclotron frequency and corresponds to the position along a field line. The horizontal axis is the real frequency of a wave that satisfies the cold plasma dispersion relation with $k_{\perp} = 0$. The twelve contour levels shown are, relative to the maximum, -0.9

to 0.9 in steps of 0.2 and the contour levels 0.01 and 0.001. The frequency corresponding to the maximum growth rate is only sensitive to changes in the ECRH frequency. This is consistent with experimental observations.

Fig. 14. Characteristics of the instability as a function of T_χ , with $T_\chi/T_{\eta_+} = 20$ and $T_\chi/T_{\eta_-} = 10$. a) $f_{i,max}$, b) $f_{r,max}$, c) $k_{i,max}/2\pi$, d) $k_{r,max}/2\pi$, e) $f_{c,max}$ and f) average particle kinetic energy $\frac{1}{2} \int v^2 f dv$. In this and succeeding figures parameters subscripted with “max” is the value of that parameter for the maximum f_i (i.e. the highest contour in plots of the type shown in Fig 13).

Fig. 15. Characteristics of the instability as a function of T_χ/T_{η_+} , with $T_{\eta_+}/T_{\eta_-} = 2$ constant. a) $f_{i,max}$, b) $f_{r,max}$, c) $k_{i,max}/2\pi$, d) $k_{r,max}/2\pi$, e) $f_{c,max}$ and f) average particle kinetic energy.

Fig. 16. Characteristics of the instability as a function of midplane cyclotron frequency with an ECRH frequency of 10.5 GHz. a) $f_{i,max}$, b) $f_{r,max}$, c) $k_{i,max}/2\pi$, d) $k_{r,max}/2\pi$, e) $f_{c,max}$ and f) average particle kinetic energy.

Fig. 17. Characteristics of the instability as a function of ECRH frequency with a midplane cyclotron frequency of 8.4 GHz. a) $f_{i,max}$, b) $f_{r,max}$, c) $k_{i,max}/2\pi$, d) $k_{r,max}/2\pi$, e) $f_{c,max}$.

Fig. 18. Characteristics of the instability as a function of total midplane density, holding the ratio of the warm electron density to the total electron density at 0.1. a) $f_{i,max}$, b) $f_{r,max}$, c) $k_{i,max}/2\pi$, d) $k_{r,max}/2\pi$, e) $f_{c,max}$.

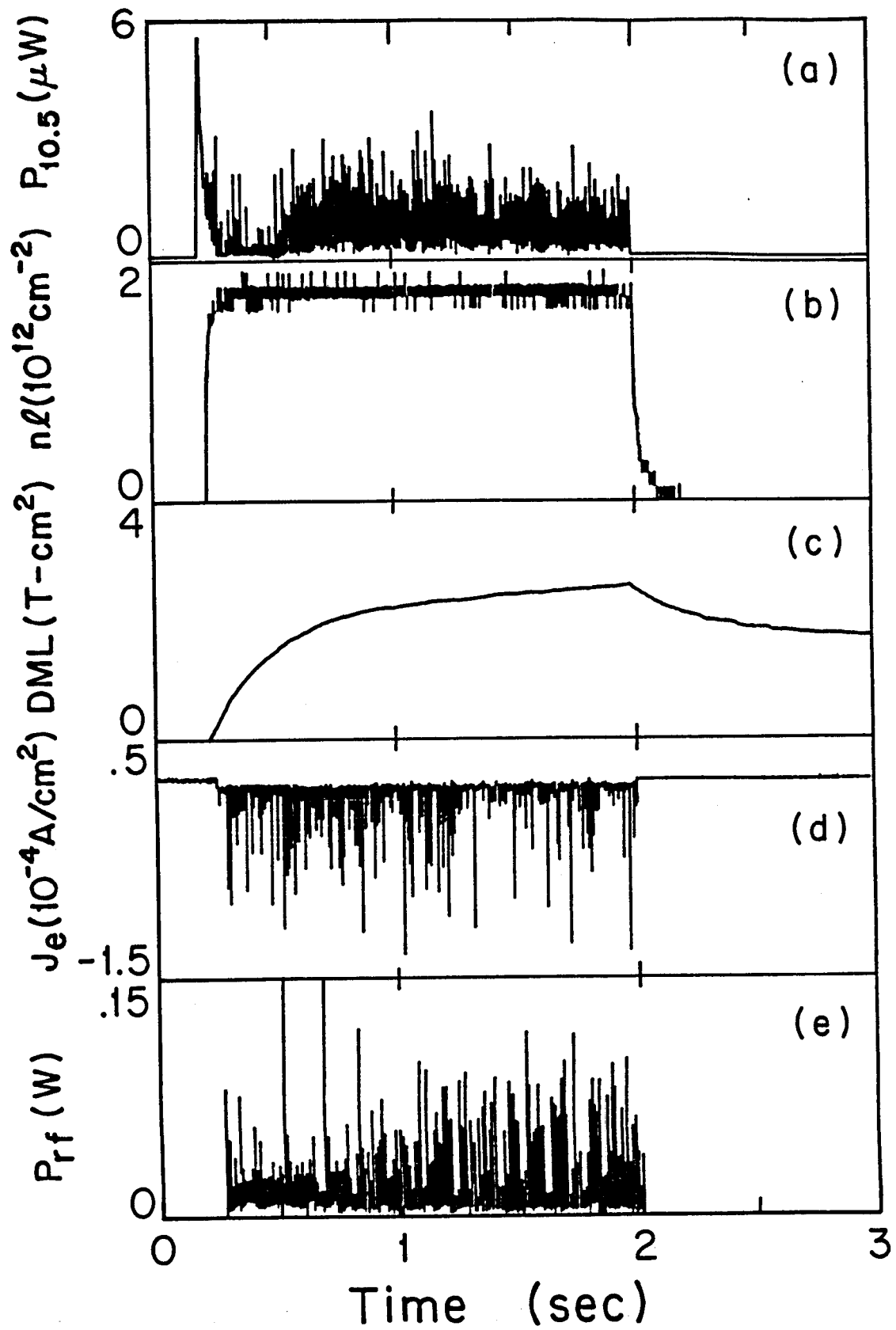


Fig. 1

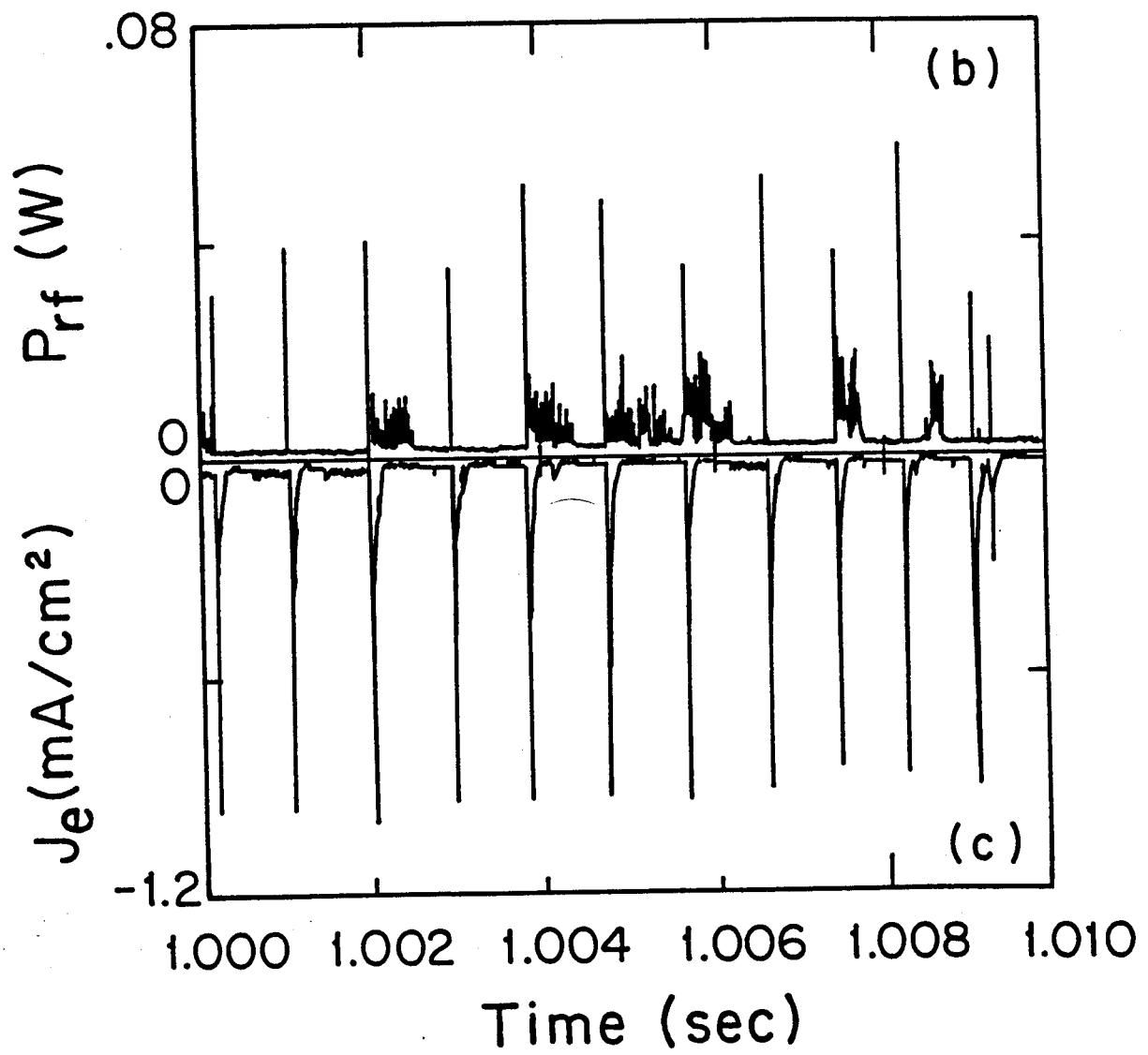
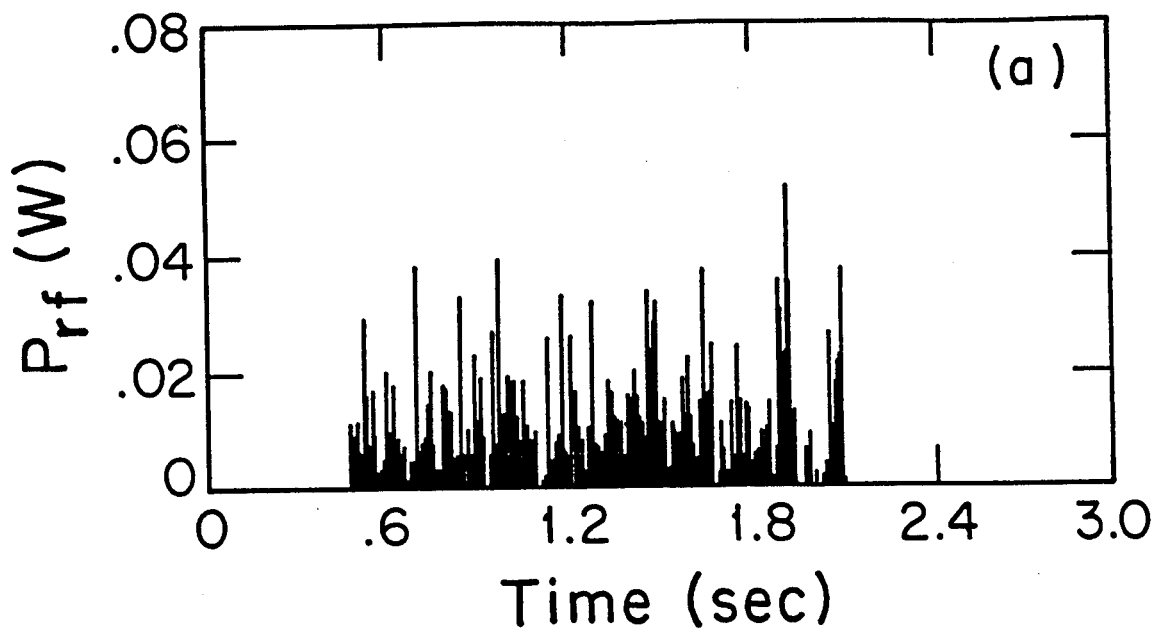


Fig. 2

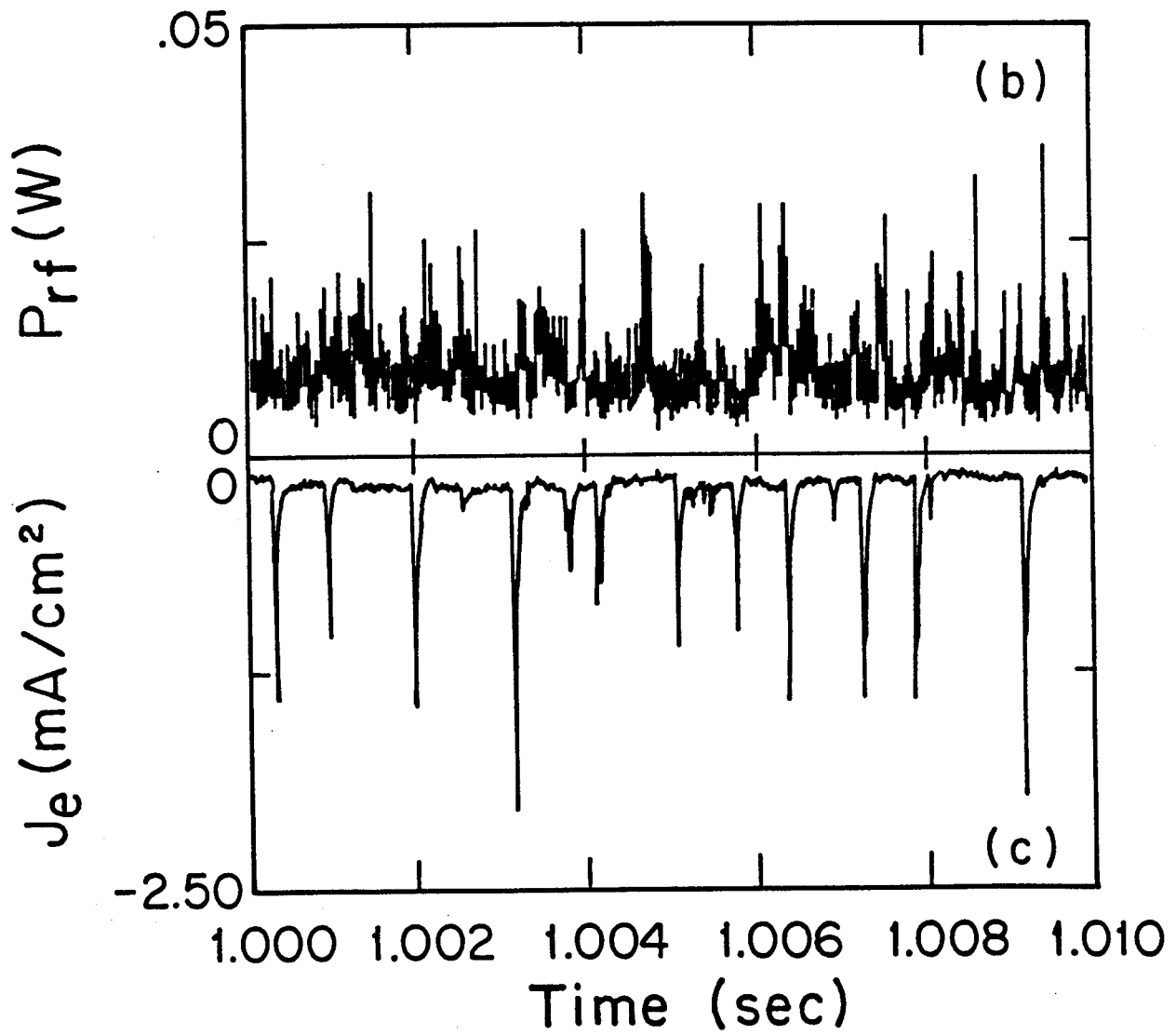
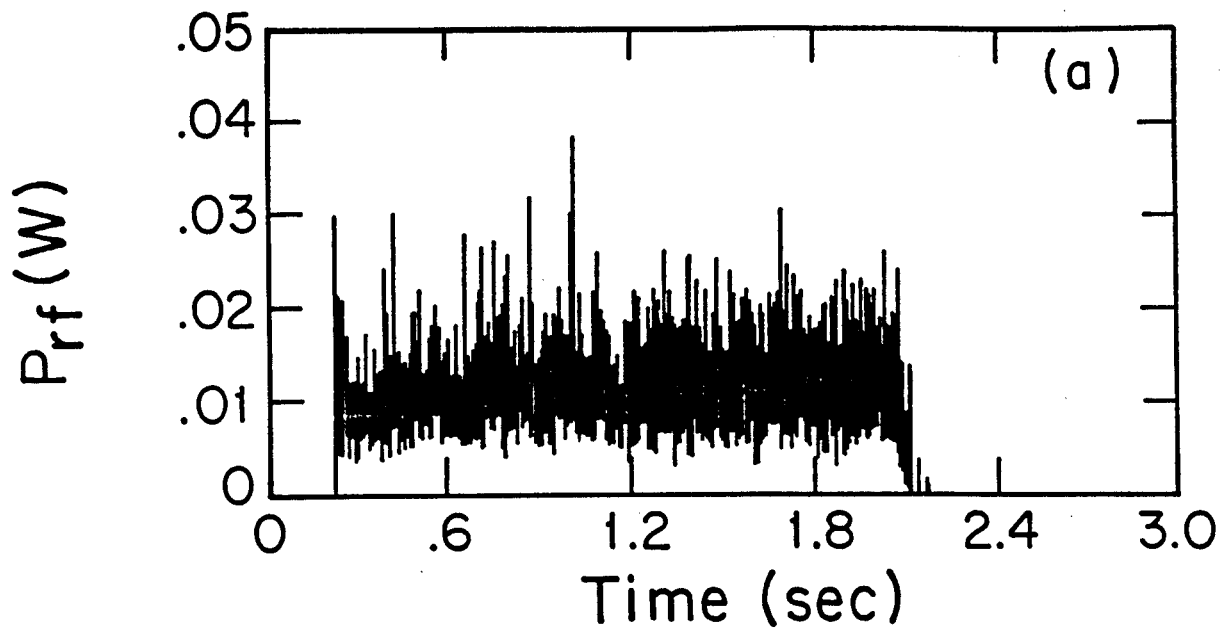


Fig. 3

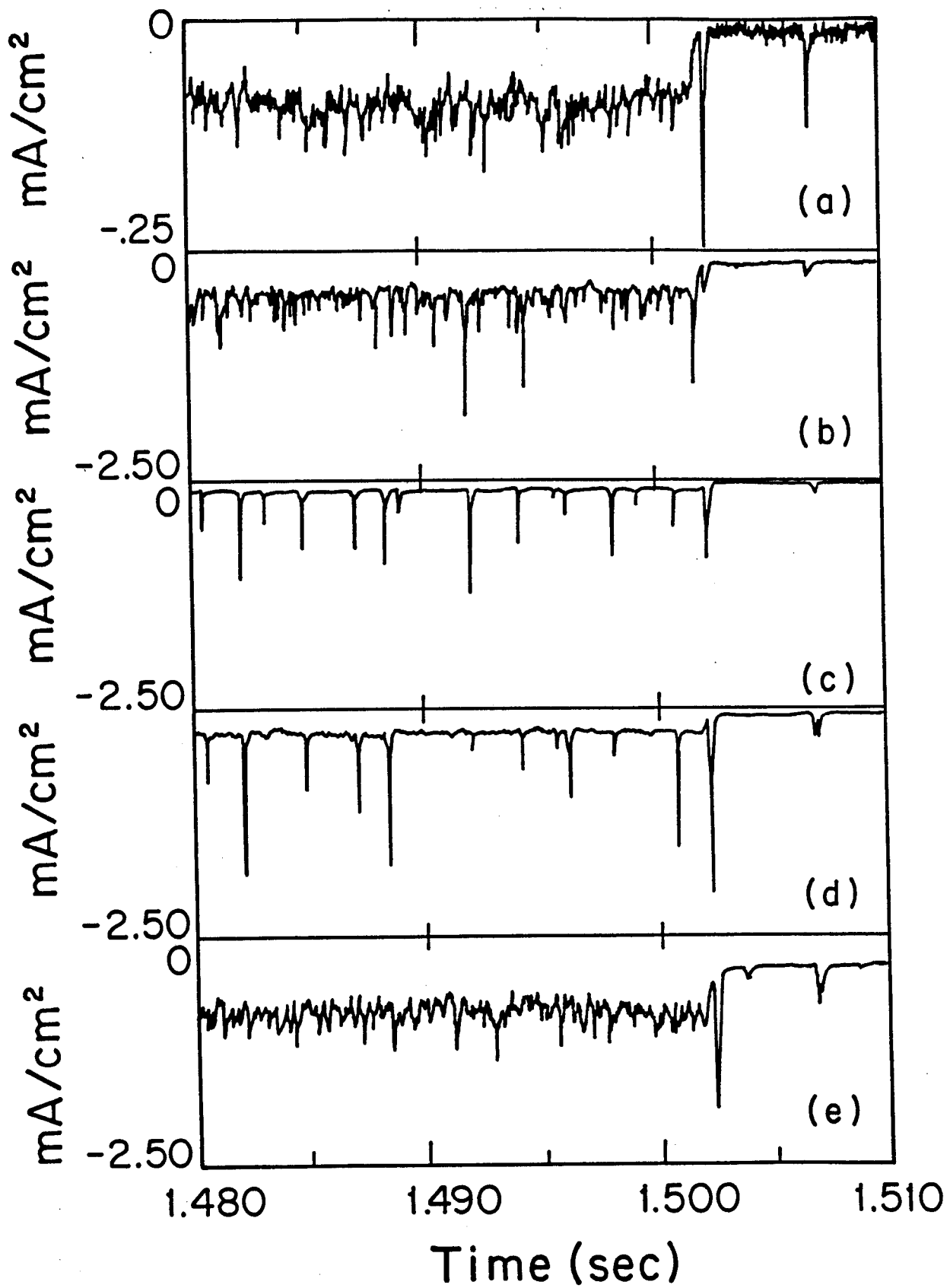


Fig. 4

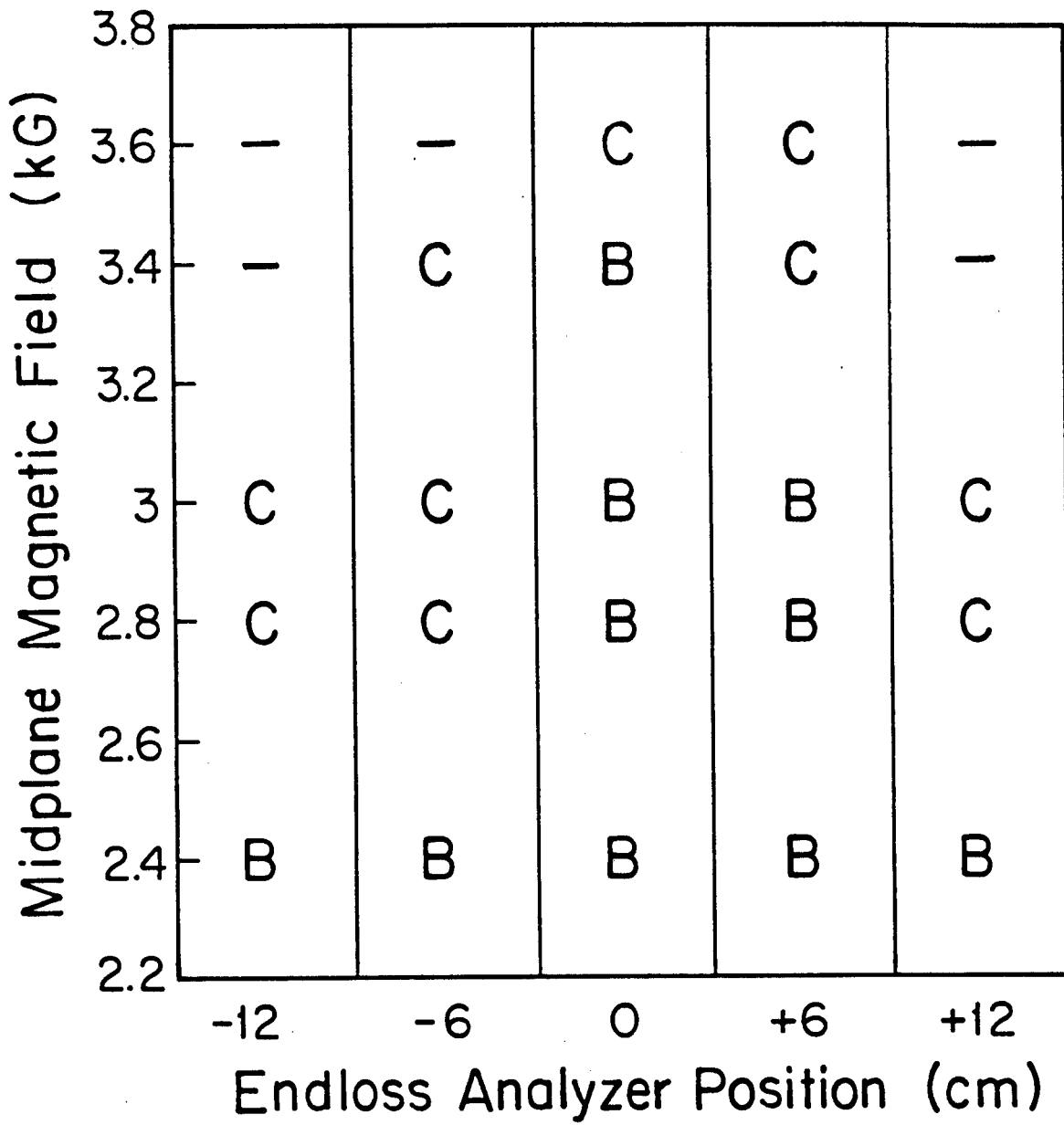


Fig. 5

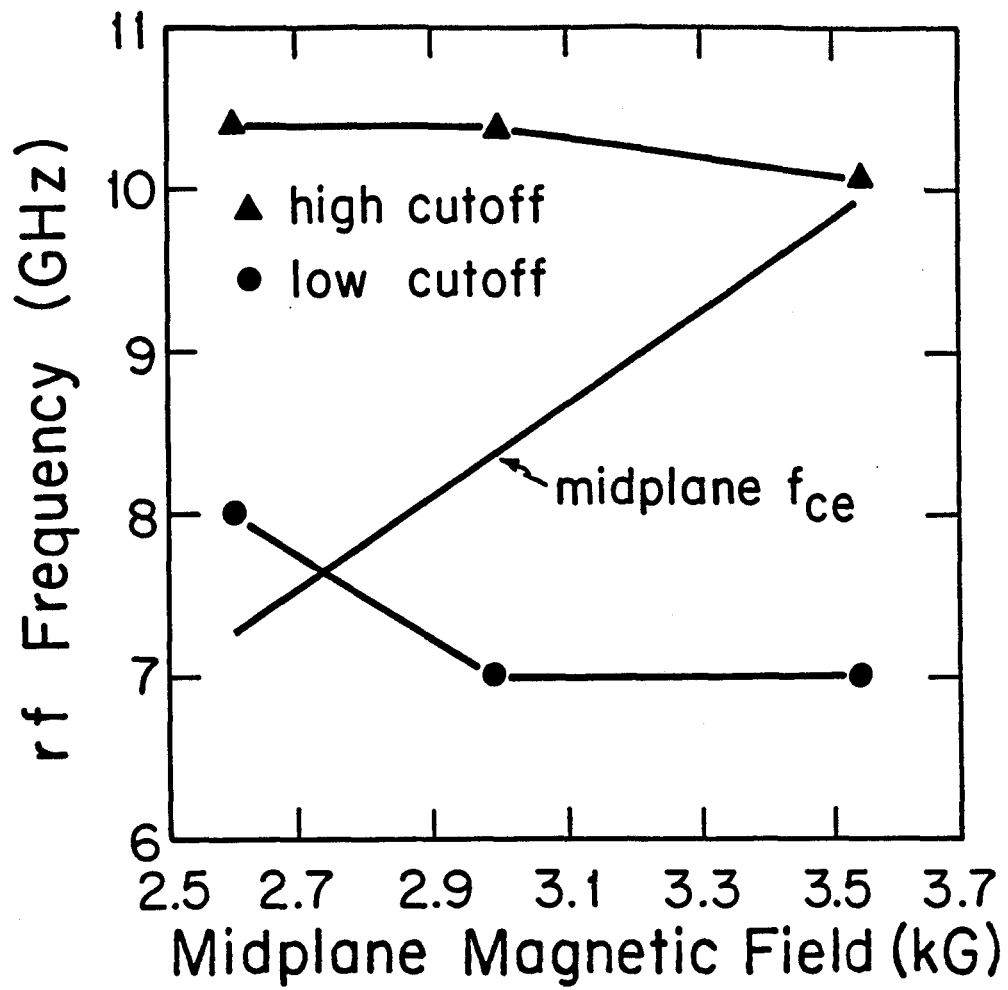


Fig. 6

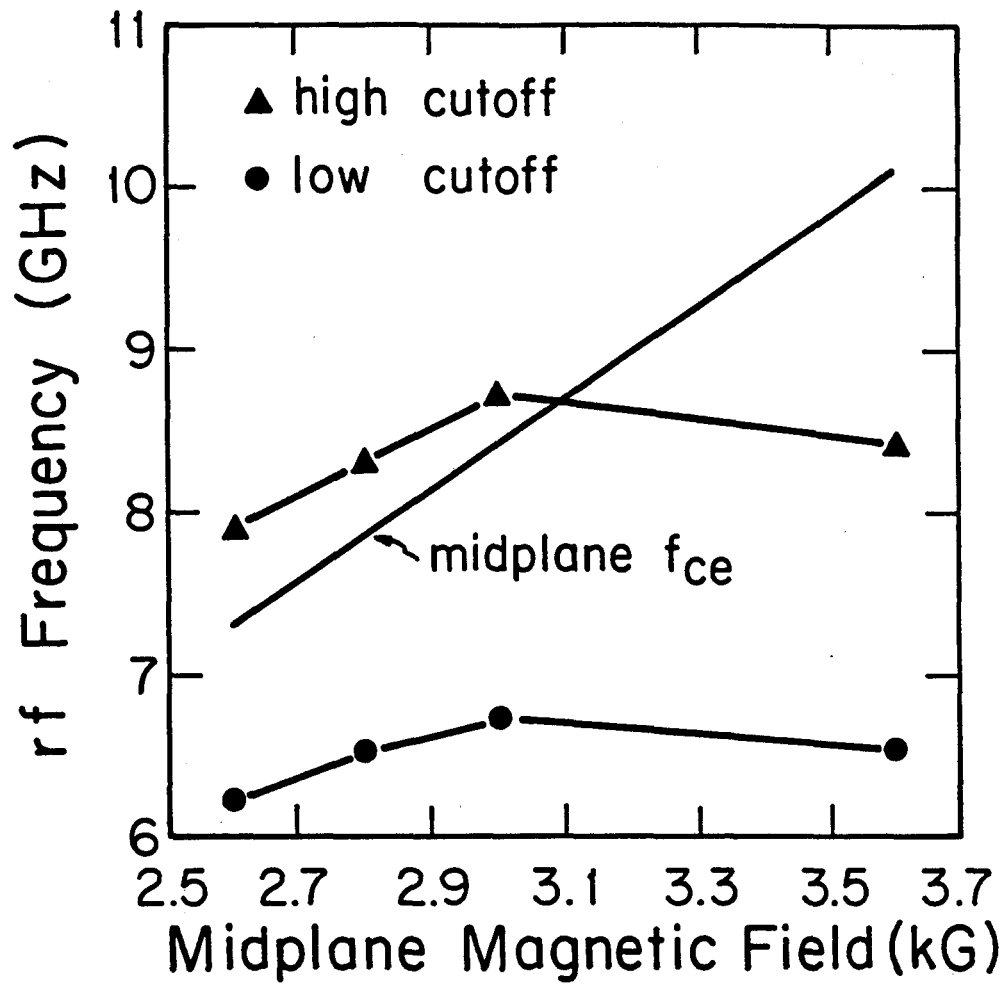


Fig. 7

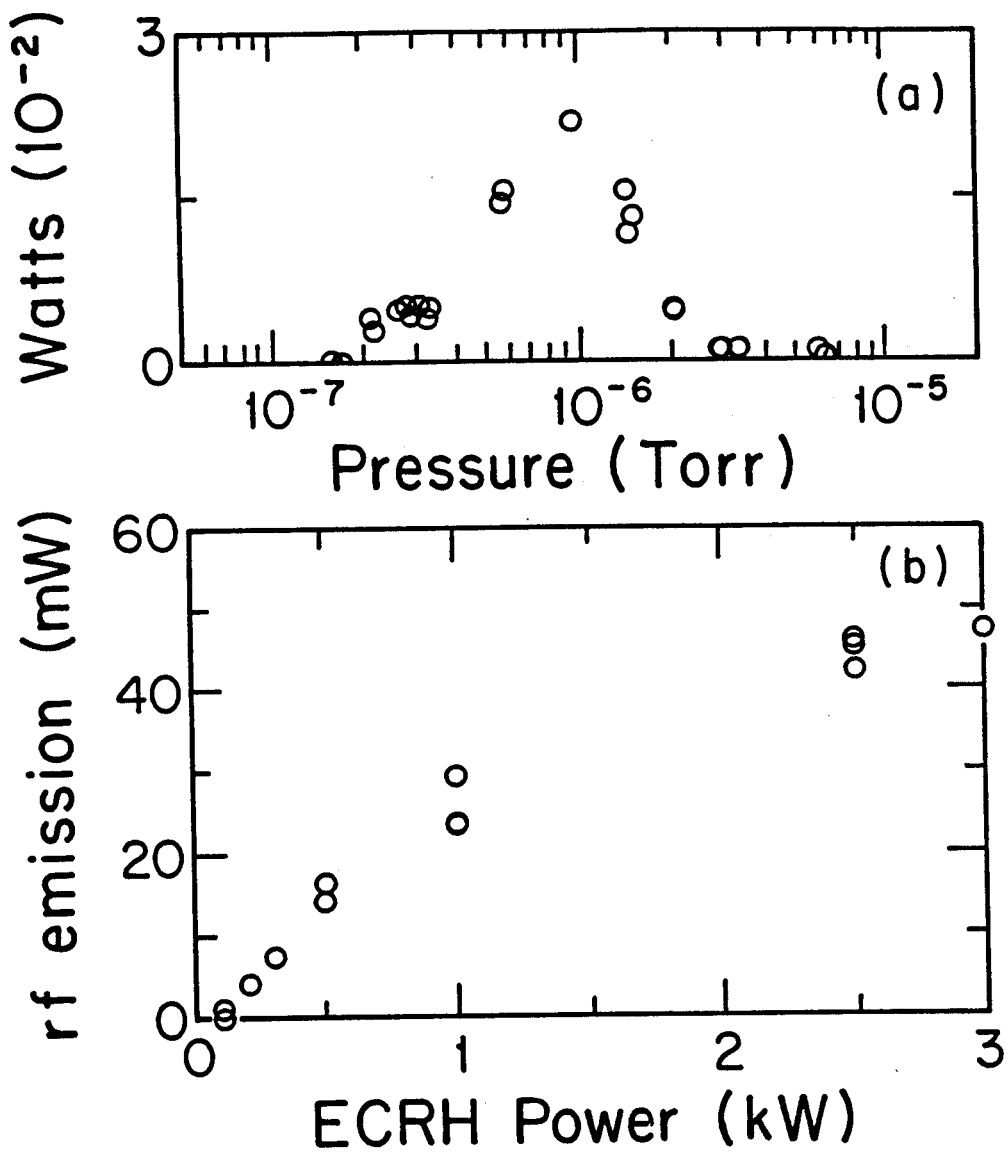


Fig. 8

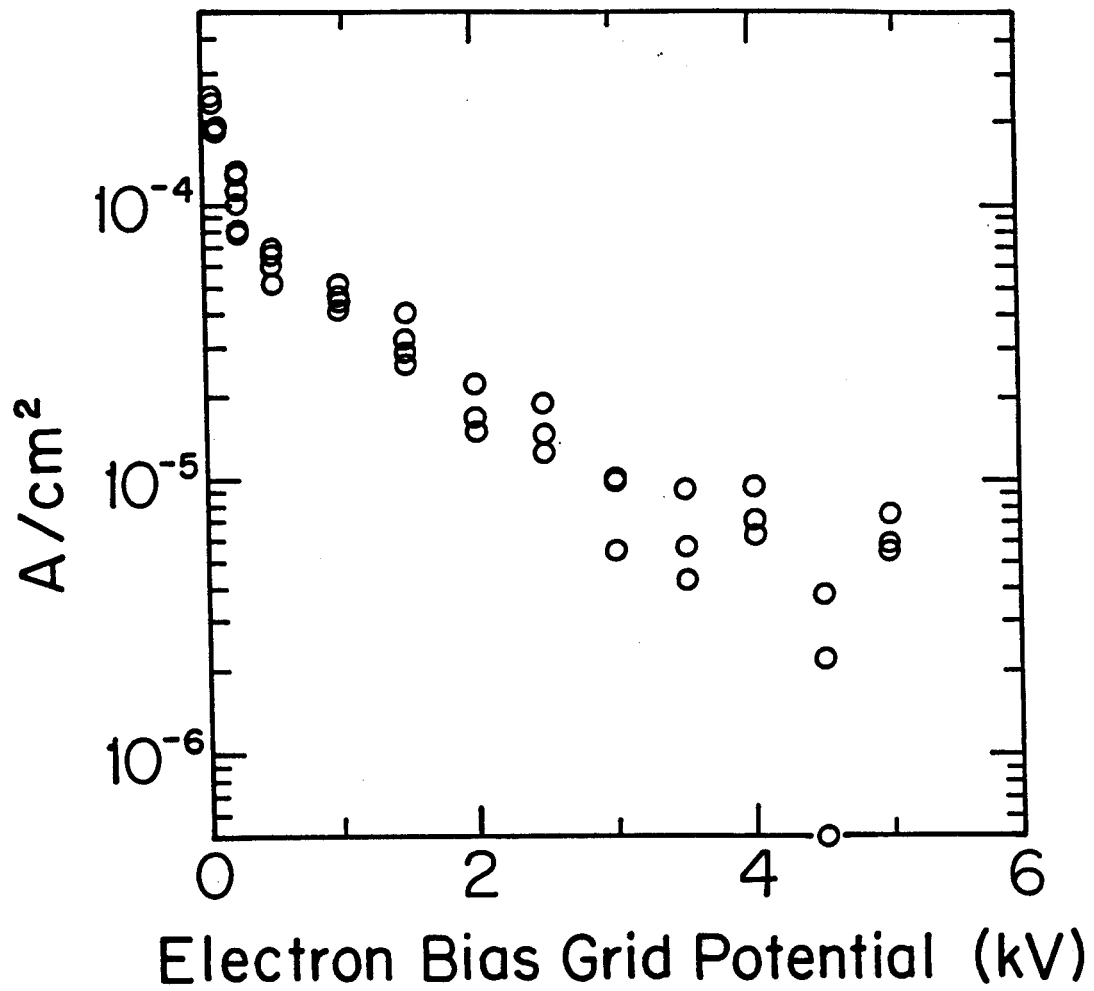


Fig. 9

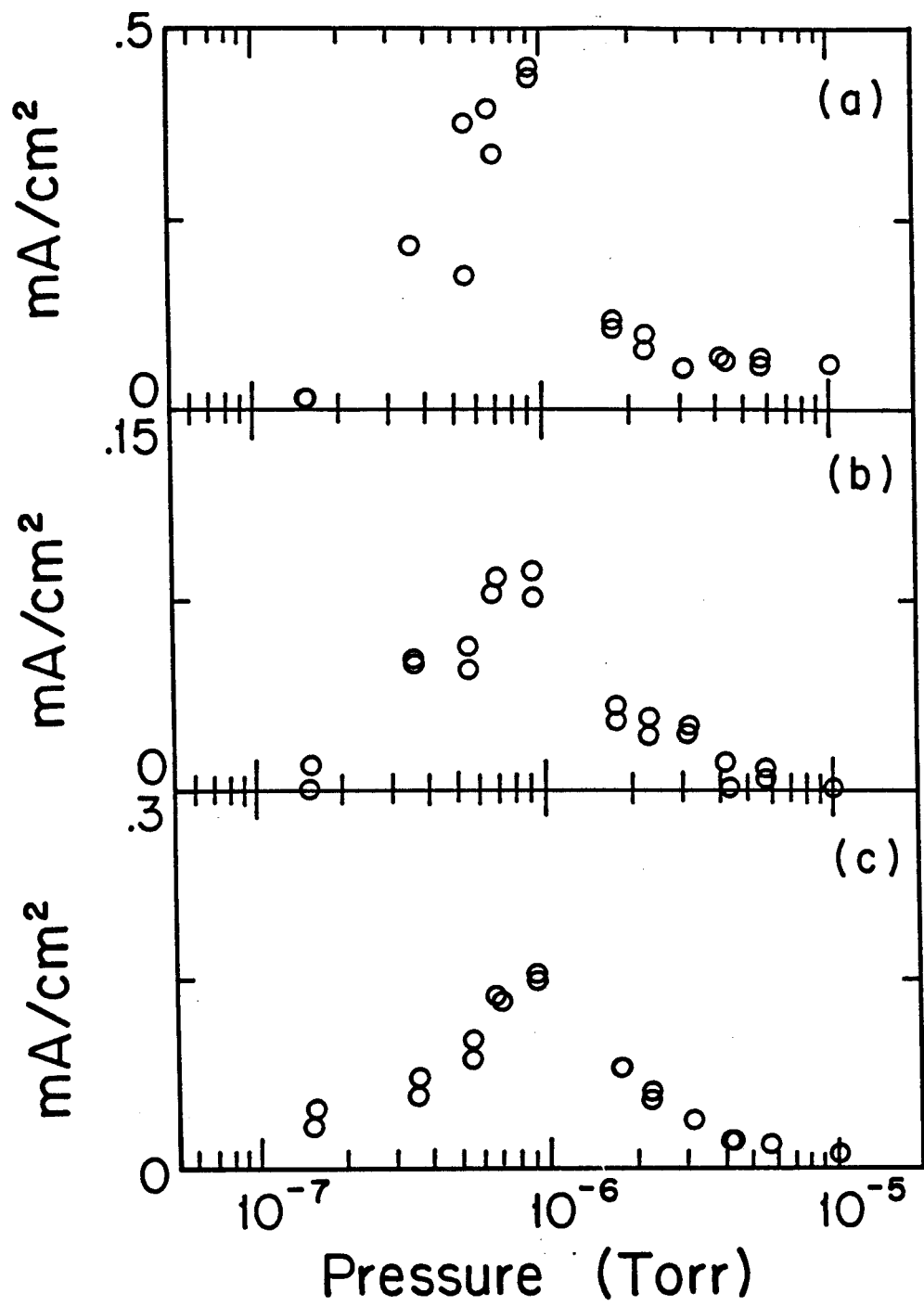


Fig. 10

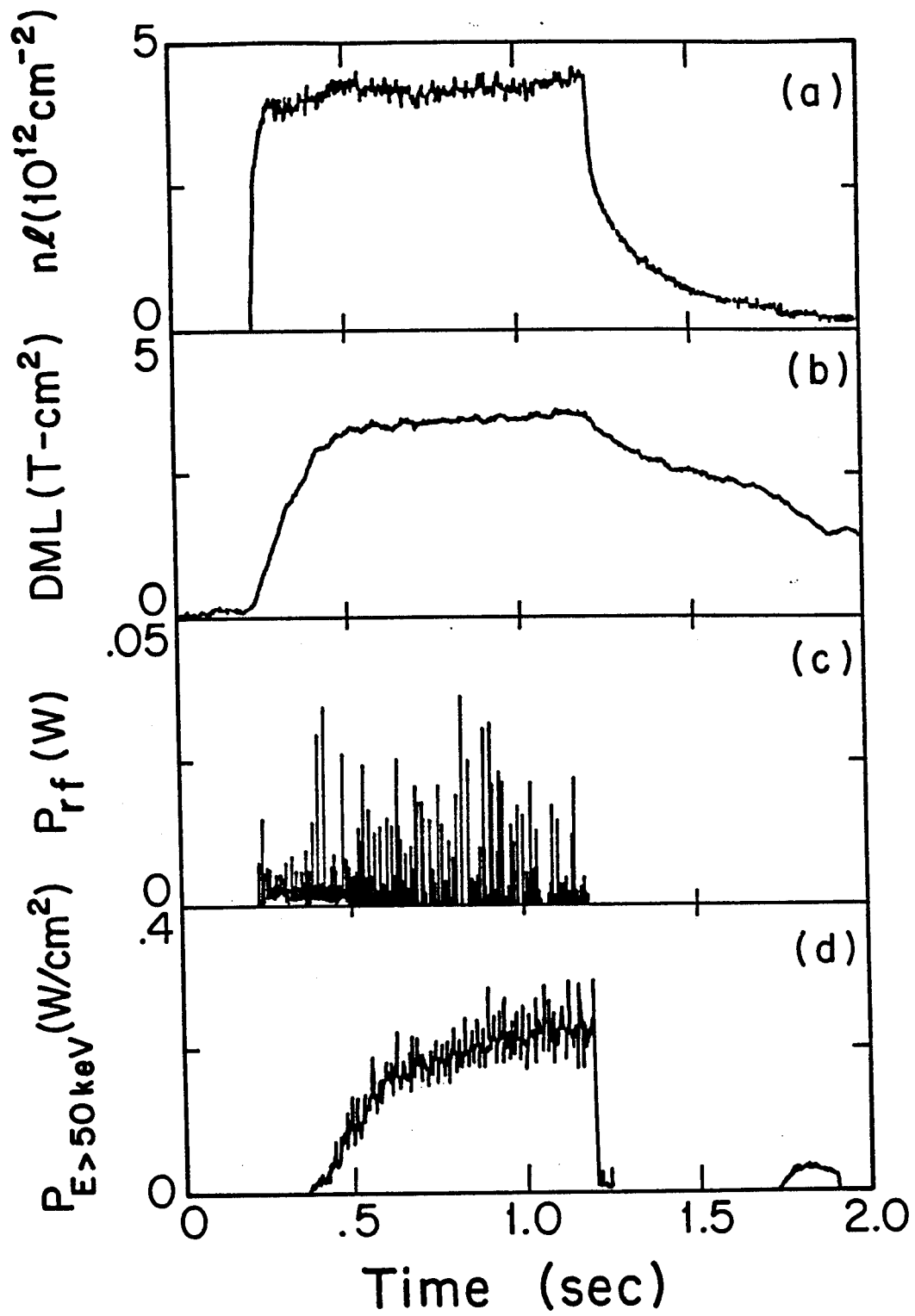


Fig. 11

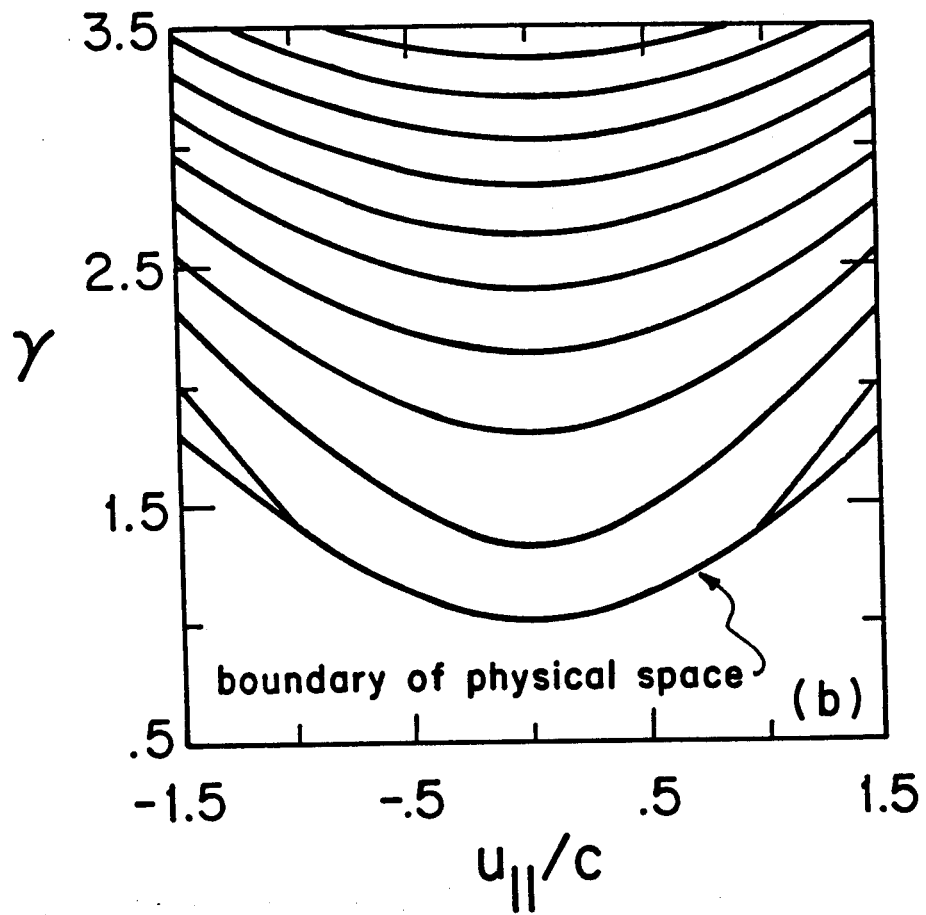
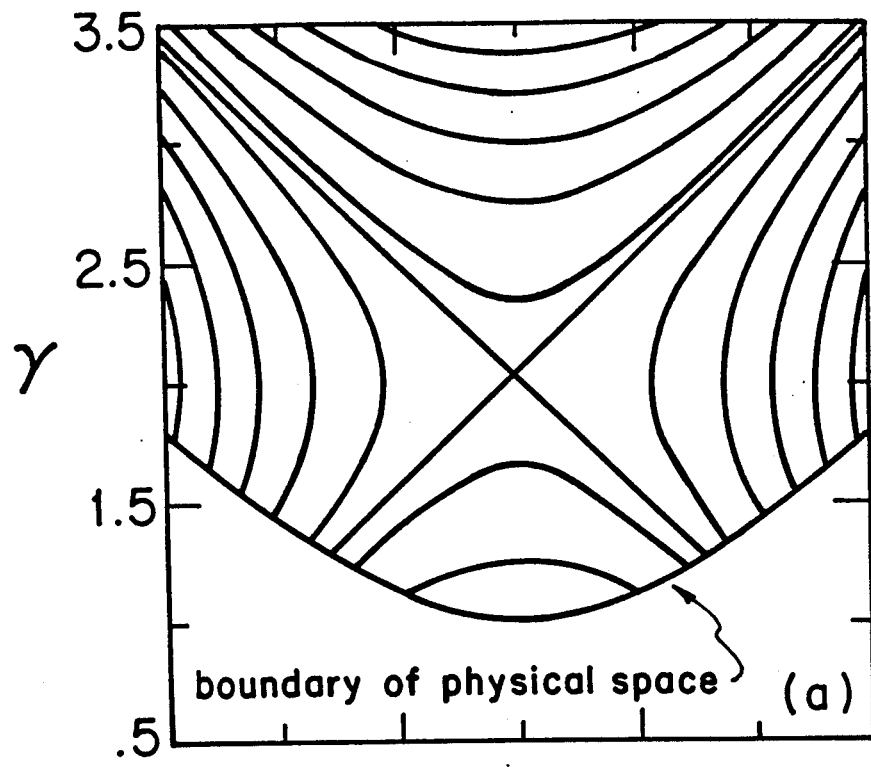


Fig. 12

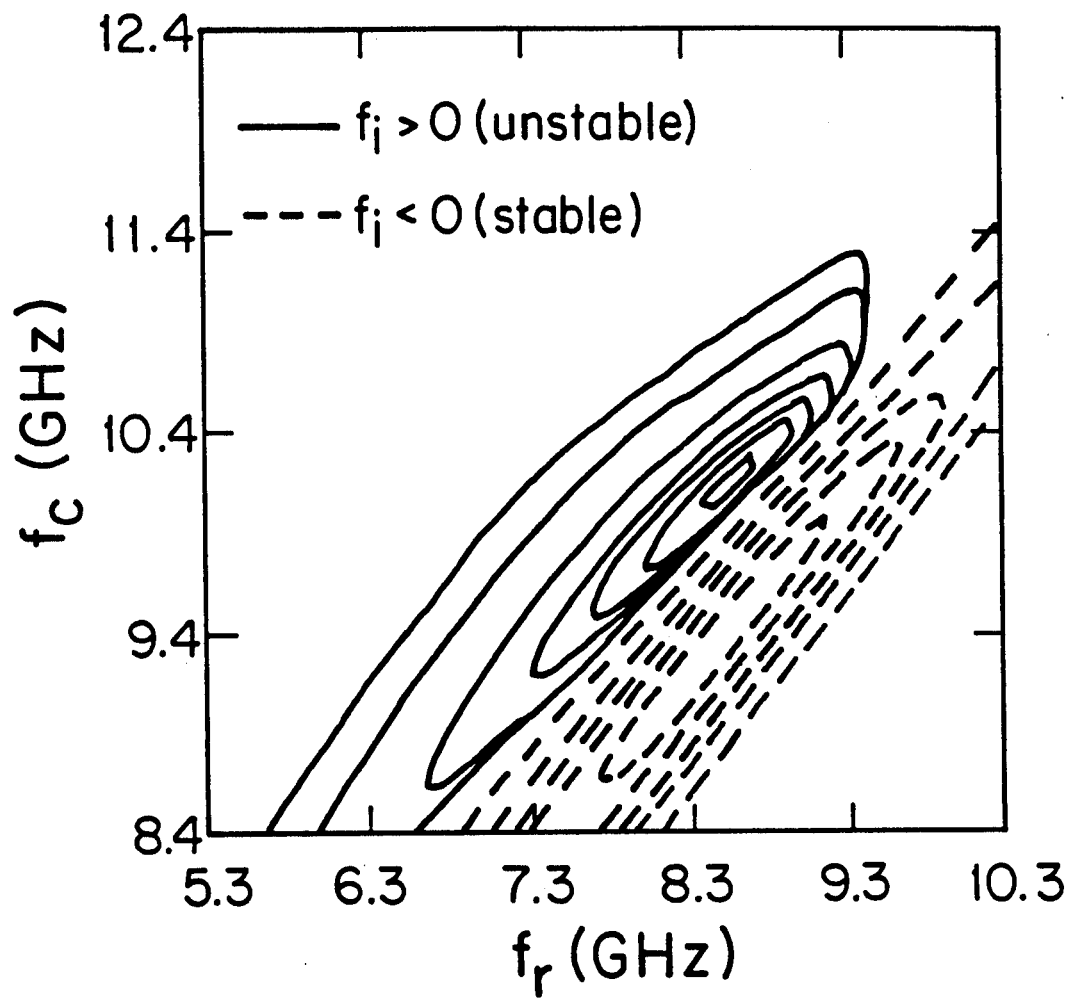


Fig. 13

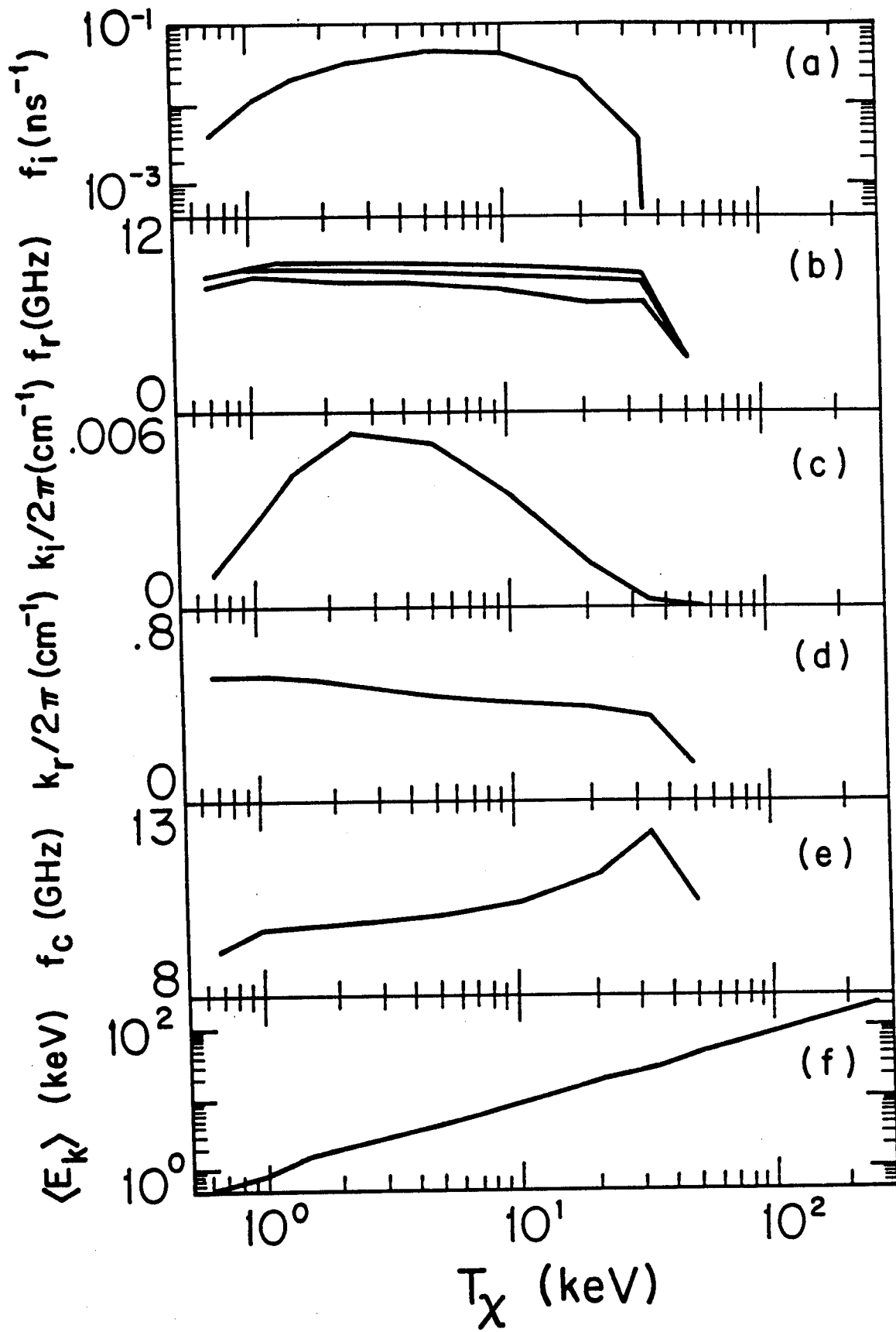


Fig. 14

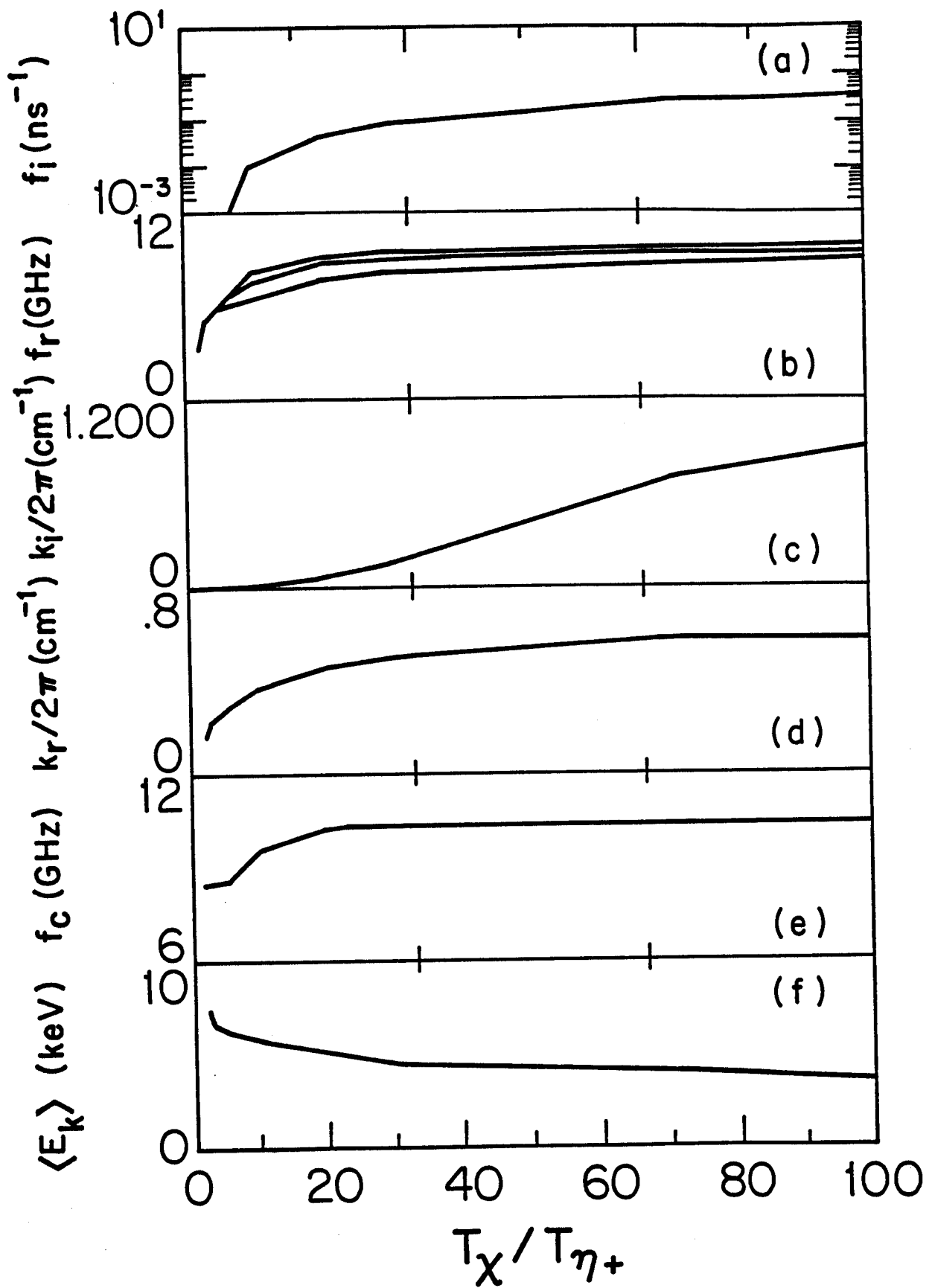


Fig. 15

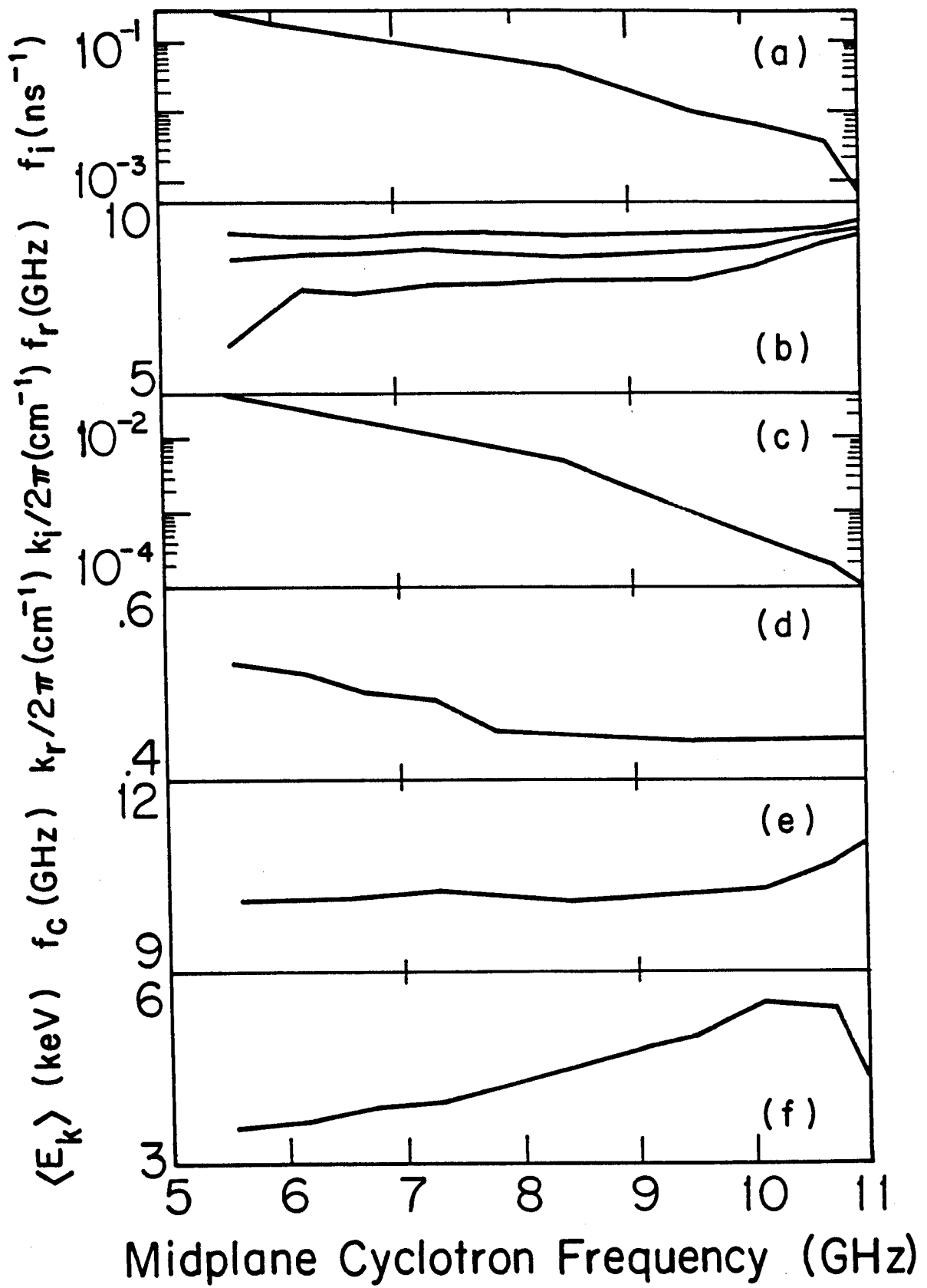


Fig. 16

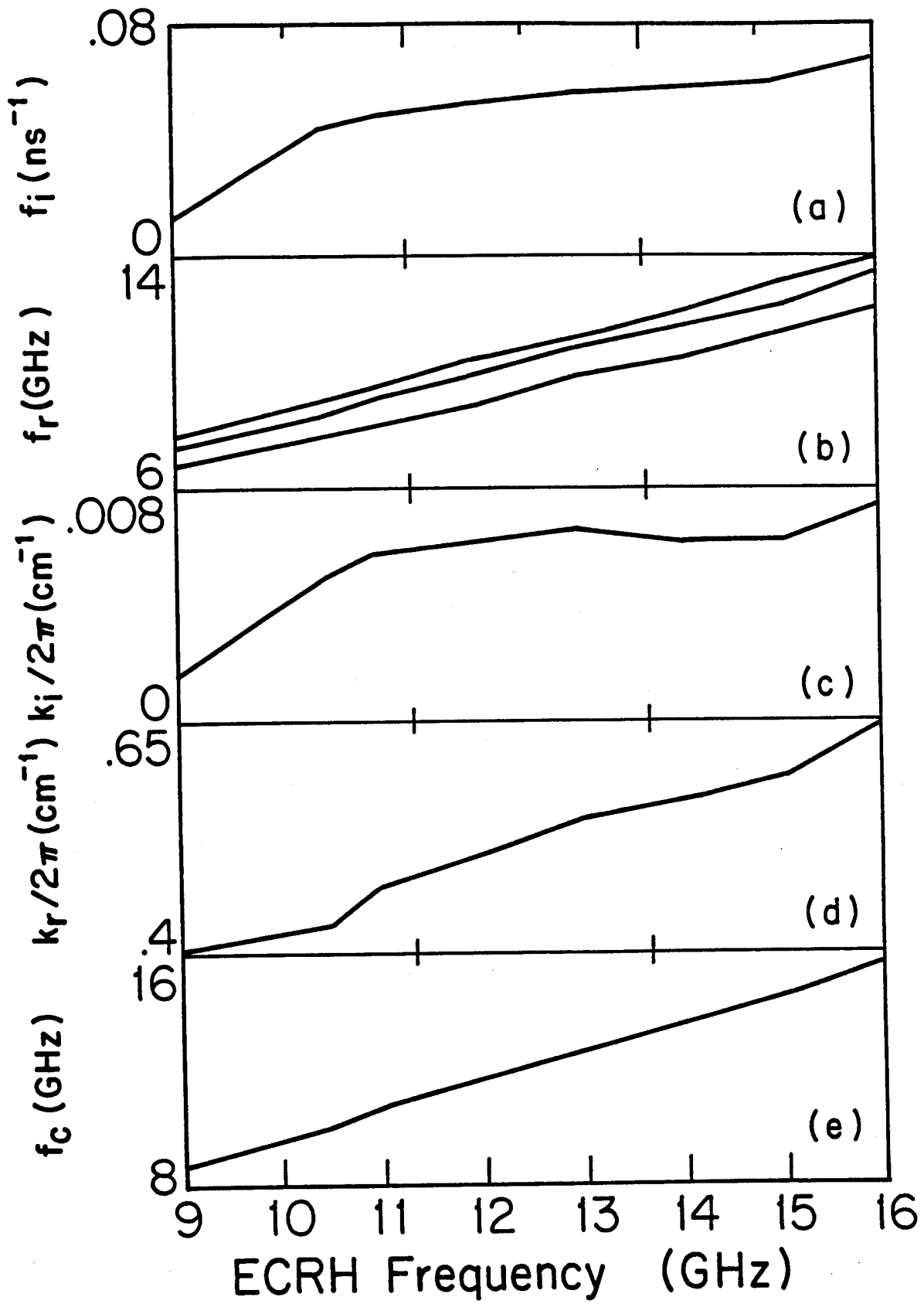


Fig. 17

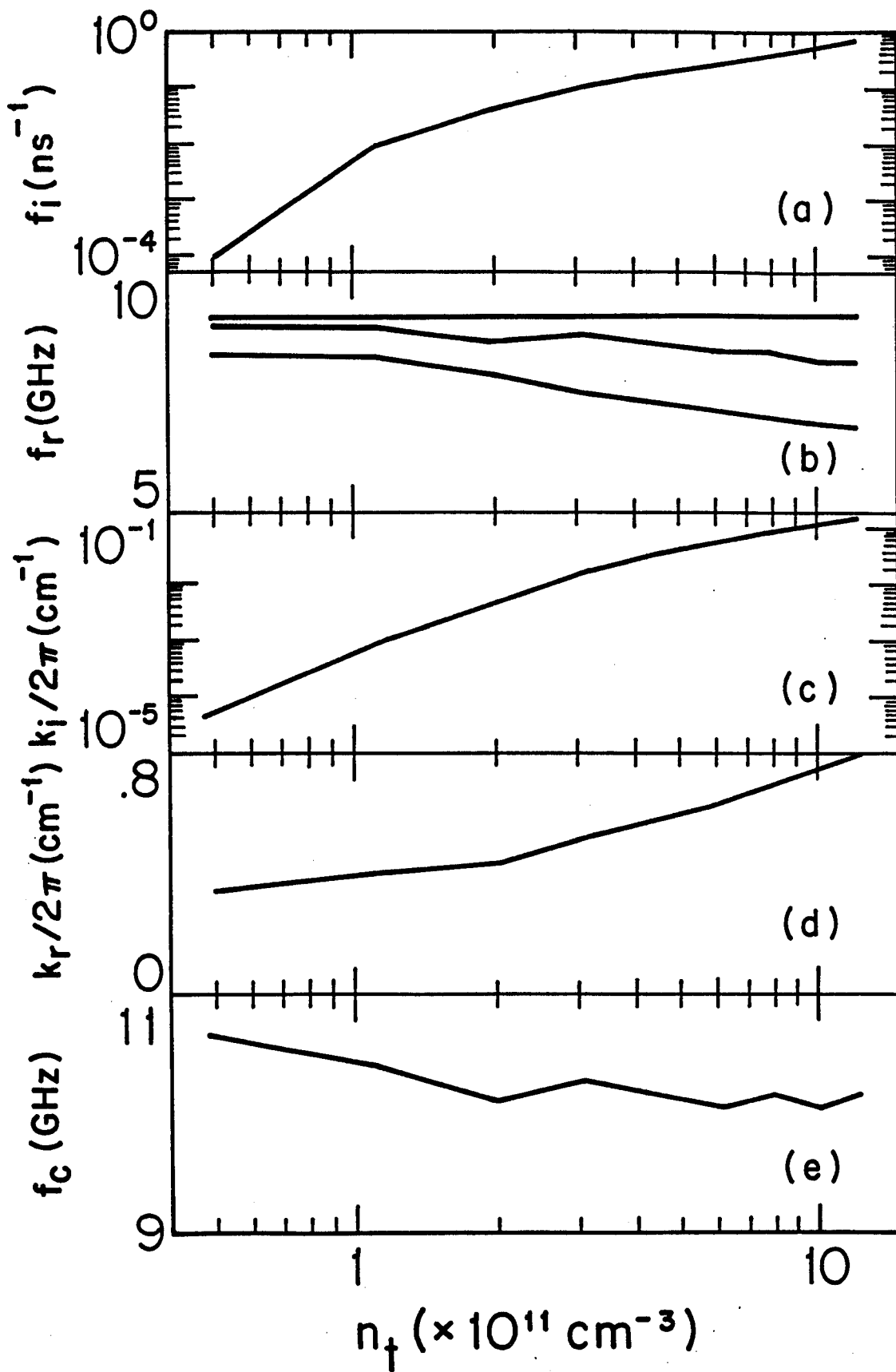


Fig. 18